TU Delft

Delft University of Technology

Realization of a minimal Kitaev chain in coupled quantum dots

Dvir, Tom; Wang, Guanzhong; van Loo, Nick; Liu, Chun Xiao; Mazur, Grzegorz P.; Bordin, Alberto; ten Haaf, Sebastiaan L.D.; van Driel, David; Zatelli, Francesco; Li, Xiang

DOI
10.1038/s41586-022-05585-1

Publication date
2023

Document Version
Final published version

Published in
Nature

Citation (APA)
Dvir, T., Wang, G., van Loo, N., Liu, C. X., Mazur, G. P., Bordin, A., ten Haaf, S. L. D., van Driel, D., Zatelli, F., Li, X., Malinowski, F. K., Gazibegovic, S., Badawy, G., Bakkers, E. P. A. M., Wimmer, M., & Kouwenhoven, L. P. (2023). Realization of a minimal Kitaev chain in coupled quantum dots. *Nature*, *614*(7948), 445-450. https://doi.org/10.1038/s41586-022-05585-1

Important note
To cite this publication, please use the final published version (if applicable).
Please check the document version above.

Copyright
Other than for strictly personal use, it is not permitted to download, forward or distribute the text or part of it, without the consent of the author(s) and/or copyright holder(s), unless the work is under an open content license such as Creative Commons.

Takedown policy
Please contact us and provide details if you believe this document breaches copyrights.
We will remove access to the work immediately and investigate your claim.

This work is downloaded from Delft University of Technology.
For technical reasons the number of authors shown on this cover page is limited to a maximum of 10.

Green Open Access added to TU Delft Institutional Repository

'You share, we take care!' - Taverne project

https://www.openaccess.nl/en/you-share-we-take-care

Otherwise as indicated in the copyright section: the publisher is the copyright holder of this work and the author uses the Dutch legislation to make this work public.

Article

Realization of a minimal Kitaev chain in coupled quantum dots

https://doi.org/10.1038/s41586-022-05585-1

Received: 16 June 2022

Accepted: 22 November 2022

Published online: 15 February 2023

Check for updates

Tom Dvir[1,2,4]✉, Guanzhong Wang[1,2,4], Nick van Loo[1,2,4], Chun-Xiao Liu[1,2], Grzegorz P. Mazur[1,2], Alberto Bordin[1,2], Sebastiaan L. D. ten Haaf[1,2], Ji-Yin Wang[1,2], David van Driel[1,2], Francesco Zatelli[1,2], Xiang Li[1,2], Filip K. Malinowski[1,2], Sasa Gazibegovic[3], Ghada Badawy[3], Erik P. A. M. Bakkers[3], Michael Wimmer[1,2] & Leo P. Kouwenhoven[1,2]✉

Majorana bound states constitute one of the simplest examples of emergent non-Abelian excitations in condensed matter physics. A toy model proposed by Kitaev shows that such states can arise at the ends of a spinless *p*-wave superconducting chain[1]. Practical proposals for its realization[2,3] require coupling neighbouring quantum dots (QDs) in a chain through both electron tunnelling and crossed Andreev reflection[4]. Although both processes have been observed in semiconducting nanowires and carbon nanotubes[5–8], crossed-Andreev interaction was neither easily tunable nor strong enough to induce coherent hybridization of dot states. Here we demonstrate the simultaneous presence of all necessary ingredients for an artificial Kitaev chain: two spin-polarized QDs in an InSb nanowire strongly coupled by both elastic co-tunnelling (ECT) and crossed Andreev reflection (CAR). We fine-tune this system to a sweet spot where a pair of poor man's Majorana states is predicted to appear. At this sweet spot, the transport characteristics satisfy the theoretical predictions for such a system, including pairwise correlation, zero charge and stability against local perturbations. Although the simple system presented here can be scaled to simulate a full Kitaev chain with an emergent topological order, it can also be used imminently to explore relevant physics related to non-Abelian anyons.

Engineering Majorana bound states in condensed matter systems is an intensively pursued goal, both for their exotic non-Abelian exchange statistics and for potential applications in building topologically protected qubits[1,9,10]. The most investigated experimental approach looks for Majorana states at the boundaries of topological superconducting materials, made of hybrid semiconducting–superconducting heterostructures[11–15]. However, the widely-relied-upon signature of Majorana states, zero-bias conductance peaks, is by itself unable to distinguish topological Majorana states from other trivial zero-energy states induced by disorder and smooth gate potentials[16–21]. Both problems disrupting the formation or detection of a topological phase originate from a lack of control over the microscopic details of the electron potential landscape in these heterostructure devices.

In this work, we realize a minimal Kitaev chain[1] using two QDs coupled by means of a short superconducting–semiconducting hybrid[2]. By controlling the electrostatic potential on each of these three elements, we overcome the challenge imposed by random disorder potentials. At a fine-tuned sweet spot where Majorana states are predicted to appear, we observe end-to-end correlated conductance that signals emergent Majorana properties such as zero charge and robustness against local perturbations. We note that these Majorana states in a minimal Kitaev chain are not topologically protected and have been dubbed 'poor man's Majorana' (PMM) states[3].

Realization of a minimal Kitaev chain

The elementary building block of the Kitaev chain is a pair of spinless electronic sites coupled simultaneously by two mechanisms: ECT and CAR. Both processes are depicted in Fig. 1a. ECT involves a single electron hopping between two sites with an amplitude t. CAR refers to two electrons from both sites tunnelling back and forth into a common superconductor with an amplitude Δ (not to be confused with the superconducting gap size), forming and splitting Cooper pairs[4]. To create the two-site Kitaev chain, we use two spin-polarized QDs, in which only one orbital level in each dot is available for transport. In the absence of tunnelling between the QDs, the system is characterized by a well-defined charge state on each QD: $|n_{\mathrm{LD}}\, n_{\mathrm{RD}}\rangle$, in which $n_{\mathrm{LD}}, n_{\mathrm{RD}} \in \{0, 1\}$ are occupations of the left and right QD levels. The charge on each QD depends only on its electrochemical potential μ_{LD} or μ_{RD}, schematically shown in Fig. 1b.

In the presence of interdot coupling, the eigenstates of the combined system become superpositions of the charge states. ECT couples $|10\rangle$ and $|01\rangle$, resulting in two eigenstates of the form $\alpha|10\rangle - \beta|01\rangle$ (Fig. 1c), both with odd combined charge parity. These two bonding and antibonding states differ in energy by $2t$ when both QDs are at their charge degeneracy, that is, $\mu_{\mathrm{LD}} = \mu_{\mathrm{RD}} = 0$. Analogously, CAR couples the two even states $|00\rangle$ and $|11\rangle$ to produce bonding and antibonding eigenstates

[1]QuTech, Delft University of Technology, Delft, The Netherlands. [2]Kavli Institute of Nanoscience, Delft University of Technology, Delft, The Netherlands. [3]Department of Applied Physics, Eindhoven University of Technology, Eindhoven, The Netherlands. [4]These authors contributed equally: Tom Dvir, Guanzhong Wang and Nick van Loo. ✉e-mail: tom.dvir@gmail.com; l.p.kouwenhoven@tudelft.nl

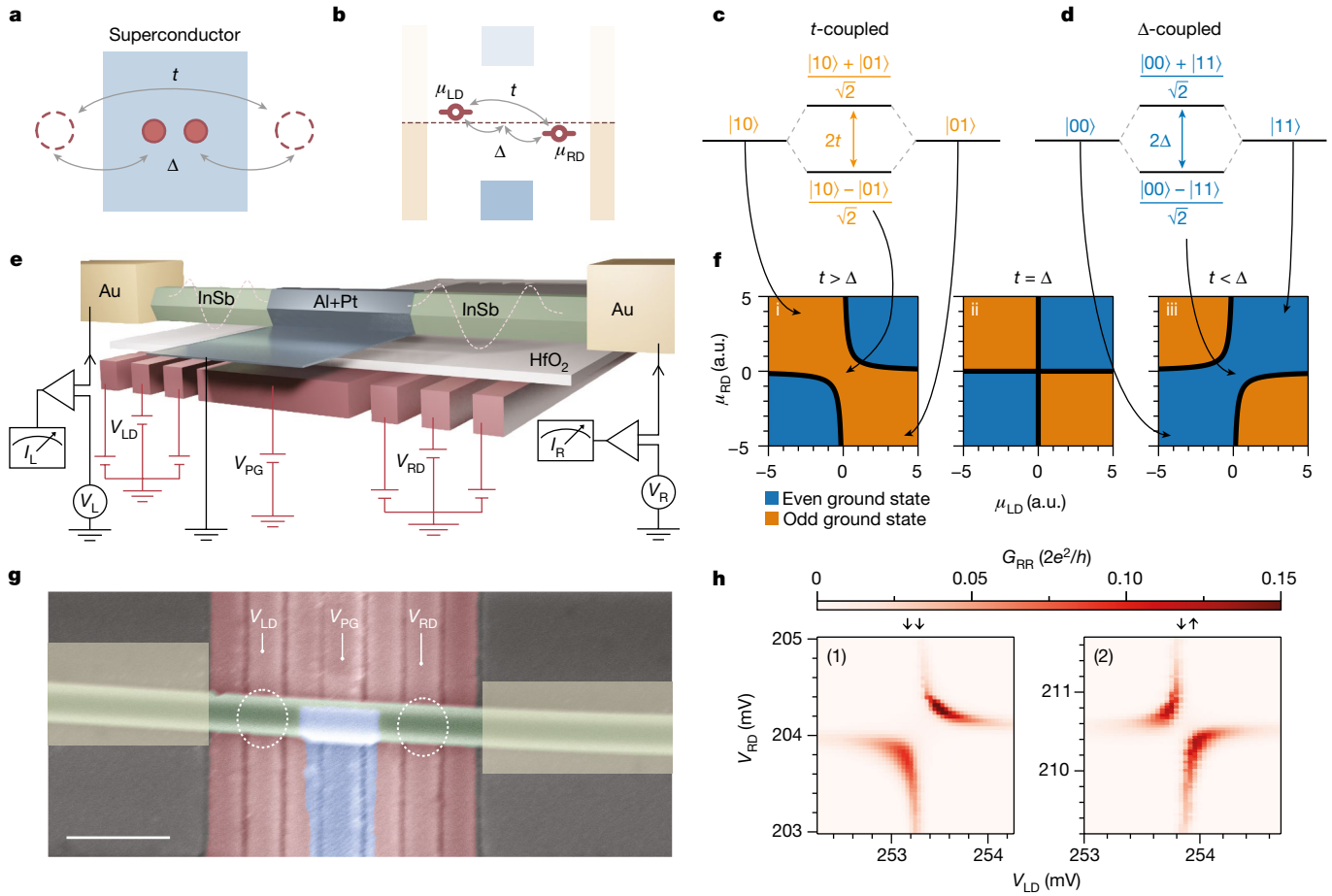


Fig. 1 | Coupling QDs through ECT and CAR. a, Illustration of the basic ingredients of a Kitaev chain: two QDs simultaneously coupled by means of ECT with amplitude t and by means of CAR with amplitude Δ through the superconductor in between. **b**, Energy diagram of a minimal Kitaev chain. Two QDs with gate-controlled chemical potentials are coupled through both ECT and CAR. The two ohmic leads enable transport measurements from both sides. **c**, Energy diagram showing that coupling the $|01\rangle$ and $|10\rangle$ states through ECT leads to a bonding state $(|10\rangle - |01\rangle)/\sqrt{2}$ and antibonding state $(|10\rangle + |01\rangle)/\sqrt{2}$. **d**, Same as **c** showing how CAR couples $|00\rangle$ and $|11\rangle$ to form the bonding state $(|00\rangle - |11\rangle)/\sqrt{2}$ and antibonding state $(|00\rangle + |11\rangle)/\sqrt{2}$. **e**, Illustration of the N-QD-S-QD-N device and the measurement circuit. Dashed potentials indicate QDs defined in the nanowire by finger gates. **f**, Charge-stability diagram of the coupled-QD system, in the cases of $t > \Delta$ (i), $t = \Delta$ (ii) and $t < \Delta$ (iii). Blue marks regions in the (μ_{LD}, μ_{RD}) plane where the ground state is even and orange where the ground state is odd. **g**, False-coloured scanning electron microscopy image of the device, before the fabrication of the N leads. InSb nanowire is coloured green. QDs are defined by bottom finger gates (in red) and their locations are circled. The gates controlling the two QD chemical potentials are labelled by their voltages, V_{LD} and V_{RD}. The central thin Al/Pt film, in blue, is grounded. The proximitized nanowire underneath is gated by V_{PG}. Two Cr/Au contacts are marked by yellow boxes. The scale bar is 300 nm. **h**, Right-side zero-bias local conductance G_{RR} in the (V_{LD}, V_{RD}) plane when the system is tuned to $t > \Delta$ (1) and $t < \Delta$ (2). The arrows mark the spin polarization of the QD levels. The DC bias voltages are kept at zero, $V_L = V_R = 0$ and an AC excitation of 6 μV RMS is applied on the right side.

of the form $u|00\rangle - v|11\rangle$, preserving the even parity of the original states. These states differ in energy by 2Δ when $\mu_{LD} = \mu_{RD} = 0$ (Fig. 1d). If the amplitude of ECT is stronger than CAR ($t > \Delta$), the odd bonding state has lower energy than the even bonding state near the joint charge degeneracy $\mu_{LD} = \mu_{RD} = 0$ (see Methods for details). The system thus features an odd ground state in a wider range of QD potentials, leading to a charge-stability diagram shown in Fig. 1f, i (ref. [22]). The opposite case of CAR dominating over ECT, that is, $t < \Delta$, leads to a charge-stability diagram shown in Fig. 1f, ii, in which the even ground state is more prominent. Fine-tuning the system such that $t = \Delta$ equalizes the two avoided crossings, inducing an even–odd degenerate ground state at $\mu_{LD} = \mu_{RD} = 0$ (Fig. 1f, iii). This degeneracy gives rise to two spatially separated PMM states, each localized at one QD[3].

Figure 1e illustrates our coupled QD system and the electronic measurement circuit. An InSb nanowire is contacted on two sides by two Cr/Au normal leads (N). A 200-nm-wide superconducting lead (S) made of a thin Al/Pt film covering the nanowire is grounded and proximitizes the central semiconducting segment. The chemical potential of the proximitized semiconductor can be tuned by the gate voltage the V_{PG}. This hybrid segment shows a hard superconducting gap accompanied by discrete, gate-tunable Andreev bound states (Extended Data Fig. 1). Two QDs are defined by finger gates underneath the nanowire. Their chemical potentials μ_{LD} and μ_{RD} are linearly tuned by voltages on the corresponding gates V_{LD} and V_{RD}. Bias voltages on the two N leads, V_L and V_R, are applied independently and currents through them, I_L and I_R, are measured separately. Transport characterization shows charging energies of 1.8 meV on the left QD and 2.3 meV on the right QD (Extended Data Fig. 1). Standard DC+AC lock-in technique allows measurement of the full conductance matrix:

$$G = \begin{pmatrix} G_{LL} & G_{LR} \\ G_{RL} & G_{RR} \end{pmatrix} = \begin{pmatrix} \frac{dI_L}{dV_L} & \frac{dI_L}{dV_R} \\ \frac{dI_R}{dV_L} & \frac{dI_R}{dV_R} \end{pmatrix}. \quad (1)$$

Measurements were conducted in a dilution refrigerator in the presence of a magnetic field $B = 200$ mT applied approximately along the nanowire axis. The combination of Zeeman splitting E_Z

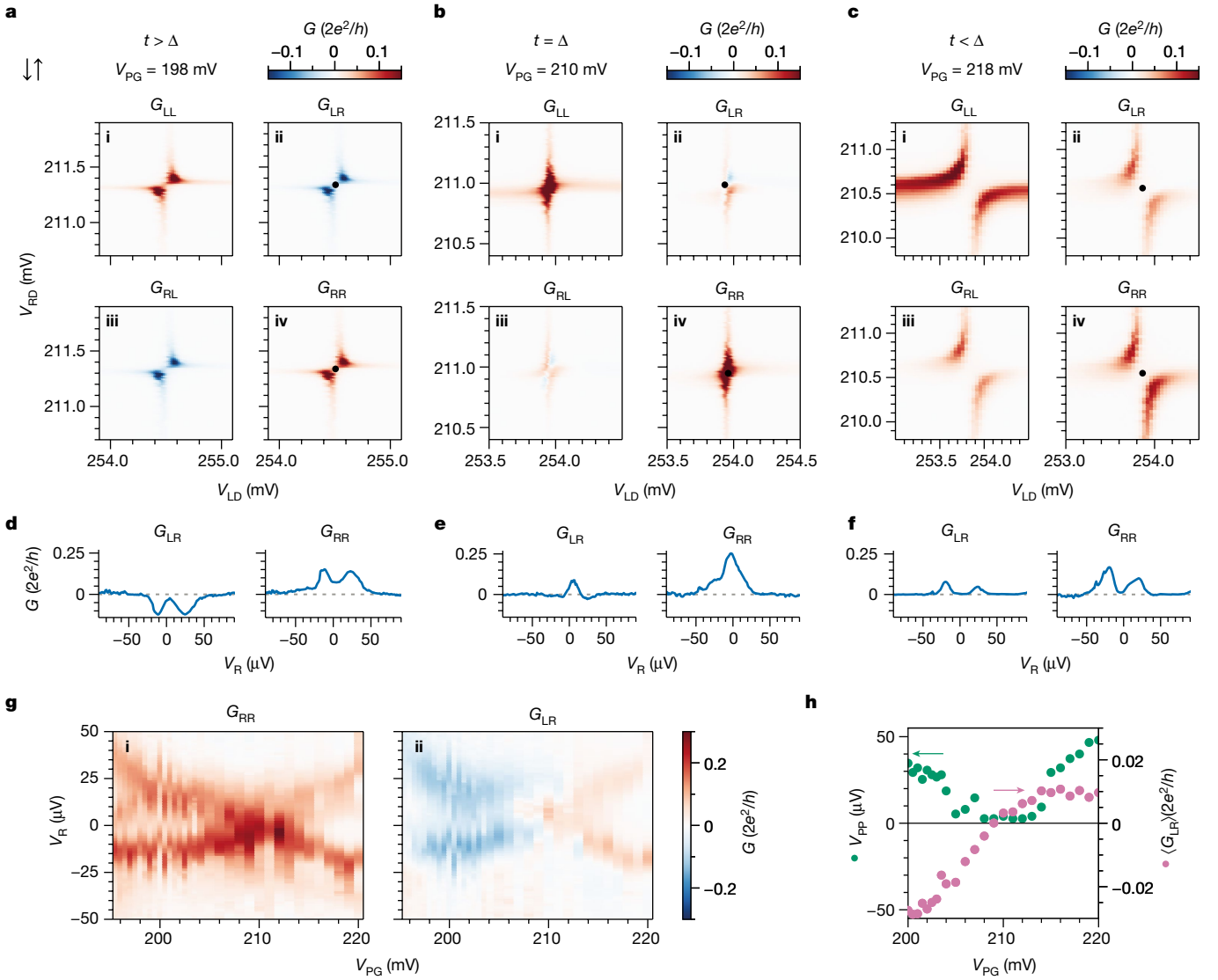


Fig. 2 | Tuning the relative strength of CAR and ECT for the ↑↓ spin configuration. a–**c**, Conductance matrices measured with V_{PG} = 198, 210 and 218 mV, respectively. **d**–**f**, G_{LR} and G_{RR} as functions of V_R when V_{LD} and V_{RD} are set to the centre of each charge-stability diagram in panels **a**–**c**, indicated by the black dots in the corresponding panels above them. **g**, Local (G_{RR}) and nonlocal (G_{LR}) conductance as a function of V_R and V_{PG} while keeping $\mu_{LD} \approx \mu_{RD} \approx 0$, showing the continuous crossover from $t > \Delta$ to $t < \Delta$. **h**, Green dots: peak-to-peak distance (V_{PP}) between the positive-bias and negative-bias segments of G_{RR}, showing the closing and reopening of QD avoided crossings. Purple dots: average G_{LR} ($\langle G_{LR} \rangle$) as a function of V_{PG}, showing a change in the sign of the nonlocal conductance.

and orbital level spacing allows single-electron QD transitions to be spin-polarized. Two neighbouring Coulomb resonances correspond to opposite spin orientations, enabling the QD spins to be either parallel (↑↑ and ↓↓) or antiparallel (↑↓ and ↓↑). We report on two devices, A in the main text and B in the extended data (Extended Data Figs. 7 and 8). A scanning electron microscopy image of device A is shown in Fig. 1g.

Transport measurements are used to characterize the charge-stability diagram of the system. In Fig. 1h, (1), we show G_{RR} as a function of QD voltages V_{LD} and V_{RD} when both QDs are set to spin-down (↓↓). The measured charge-stability diagram shows avoided crossing, which indicates the dominance of ECT. In Fig. 1h, (2), we change the spin configuration to ↓↑. The charge-stability diagram now develops the avoided crossing of the opposite orientation, indicating the dominance of CAR for QDs with antiparallel spins. This is, to our knowledge, the first verification of the prediction that spatially separated QDs can coherently hybridize through CAR coupling to a superconductor[23]. Thus we have introduced all the necessary ingredients for a two-site Kitaev chain.

Tuning the relative strength of CAR and ECT

Majorana states in long Kitaev chains are present under a wide range of parameters owing to topological protection[1]. Notably, even a chain consisting of only two sites can host a pair of PMM states despite a lack of topological protection, if the fine-tuned sweet spot $t = \Delta$ and $\mu_{LD} = \mu_{RD} = 0$ can be achieved[3]. This, however, is made challenging by the above-mentioned requirement to have both QDs spin-polarized. If spin is conserved, ECT can only take place between QDs with ↓↓ or ↑↑ spins, whereas CAR is only allowed for ↑↓ and ↓↑. Rashba spin–orbit coupling in InSb nanowires solves this dilemma[2,24,25], allowing finite ECT even in antiparallel spin configurations and CAR between QDs with equal spins.

A further challenge is to make the two coupling strengths equal for a given spin combination. References[24–26] show that both CAR and ECT in our device are virtual transitions through intermediate Andreev bound states residing in the short InSb segment underneath the superconducting film. Thus varying V_{PG} changes the energy and wavefunction

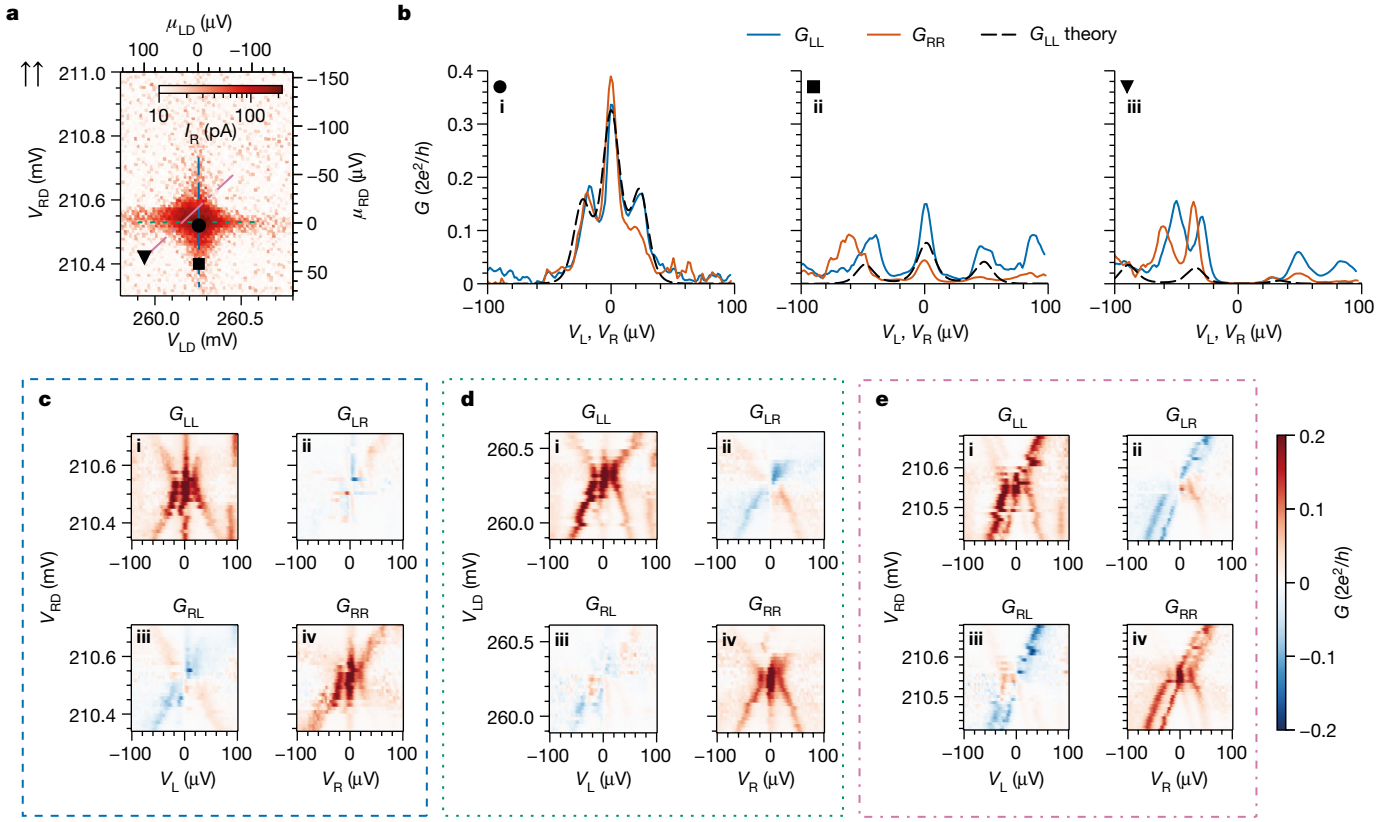


Fig. 3 | Conductance spectroscopy at the $t = \Delta$ sweet spot for the ↑↑ spin configuration. a, I_R versus V_{LD} and V_{RD} under $V_L = 0$ and $V_R = 10$ μV. The spectra in panel **b** are taken at values of V_{LD} and V_{RD} marked by corresponding symbols. The gate versus bias sweeps are taken along the dashed, dotted and dashed-dotted lines in panels **c**, **d** and **e**, respectively. Data are taken with fixed $V_{PG} = 215.1$ mV. **b**, Spectra taken under the values of V_{LD} and V_{RD} marked in panel **a**. The dashed lines are theoretical curves calculated with $t = \Delta = 12$ μeV, $\Gamma_L = \Gamma_R = 4$ μeV, $T = 45$ mK and at QD energies converted from V_{LD} and V_{RD} using measured lever arms (see Methods for details). **c**,**d**, G as a function of the applied bias and V_{RD} (**c**) or V_{LD} (**d**), taken along the paths indicated by the dashed blue line and the dotted green line in panel **a**, respectively. **e**, G as a function of the applied bias and along the diagonal indicated by the dashed-dotted pink line in panel **a**. This diagonal represents 500 μV of change in V_{LD} and 250 μV of change in V_{RD}.

of said Andreev bound states and, thereby, t and Δ. We search for the V_{PG} range over which Δ changes differently from t and look for a crossover in the type of charge-stability diagrams.

Figure 2a–c shows the resulting charge-stability diagrams for the ↓↑ spin configuration at different values of V_{PG}. The conductance matrix $G(V_L = 0, V_R = 0)$ at $V_{PG} = 198$ mV is shown in Fig. 2a. The local conductance on both sides, G_{LL} and G_{RR}, exhibit level repulsion indicative of $t > \Delta$. We emphasize that ECT can become stronger than CAR even though the spins of the two QD transitions are antiparallel because of the electric gating mentioned above. The dominance of ECT over CAR can also be seen in the negative sign of the nonlocal conductance, G_{LR} and G_{RL}. During ECT, an electron enters the system through one dot and exits through the other, resulting in negative nonlocal conductance. CAR, by contrast, causes two electrons to enter or leave both dots simultaneously, producing positive nonlocal conductance[27]. The residual finite conductance in the centre of the charge-stability diagram can be attributed to level broadening resulting from finite temperature and dot-lead coupling (see Extended Data Fig. 10). In Fig. 2d, we show the conductance spectrum measured as a function of V_R, with V_{LD} and V_{RD} tuned to $\mu_{LD} \approx \mu_{RD} \approx 0$ (black dots in Fig. 2c, ii and iv). A pair of conductance peaks or dips is visible on either side of zero energy.

Figure 2c shows G at $V_{PG} = 218$ mV (the G_{RR} component is also used for Fig. 1h, (2)). Here all the elements of G exhibit CAR-type avoided crossings. The spectrum shown in panel f, obtained at the joint charge degeneracy point (black dots in panel c, ii and iv), similarly has two conductance peaks surrounding zero energy. The measured nonlocal conductance is positive, as predicted for CAR. The existence of both $t > \Delta$ and $t < \Delta$ regimes, together with continuous gate tunability, allows us to approach the $t \approx \Delta$ sweet spot. This is shown in panel b, taken with $V_{PG} = 210$ mV. Here G_{RR} and G_{LL} exhibit no avoided crossing, whereas G_{LR} and G_{RL} fluctuate around zero, confirming that CAR and ECT are in balance. Accordingly, the spectrum in panel e confirms that the even and odd ground states are degenerate and transport can occur at zero excitation energy by means of the appearance of a zero-bias conductance peak. The crossover from the $t > \Delta$ regime to the $t < \Delta$ regime can be seen across several QD resonances (Extended Data Fig. 9).

To show that gate-tuning of the t/Δ ratio is indeed continuous, we repeat charge-stability diagram measurements (Extended Data Fig. 3) and bias spectroscopy at more V_{PG} values. As before, each bias sweep is conducted while keeping both QDs at charge degeneracy. Figure 2g shows the resulting composite plot of G_{RR} (i) and G_{LR} (ii) versus bias voltage and V_{PG}. The X-shaped conductance feature indicates a continuous evolution of the excitation energy, with a linear zero-energy crossing agreeing with predictions in ref. [3]. Following analysis described in Methods, we extract the peak spacing and average nonlocal conductance in Fig. 2h to visualize the continuous crossover from $t > \Delta$ to $t < \Delta$.

PMM sweet spot

Next we study the excitation spectrum in the vicinity of the $t = \Delta$ sweet spot. The predicted zero-temperature experimental signature of the PMM states is a pair of quantized zero-bias conductance peaks on both sides of the devices. These zero-bias peaks are persistent even when one

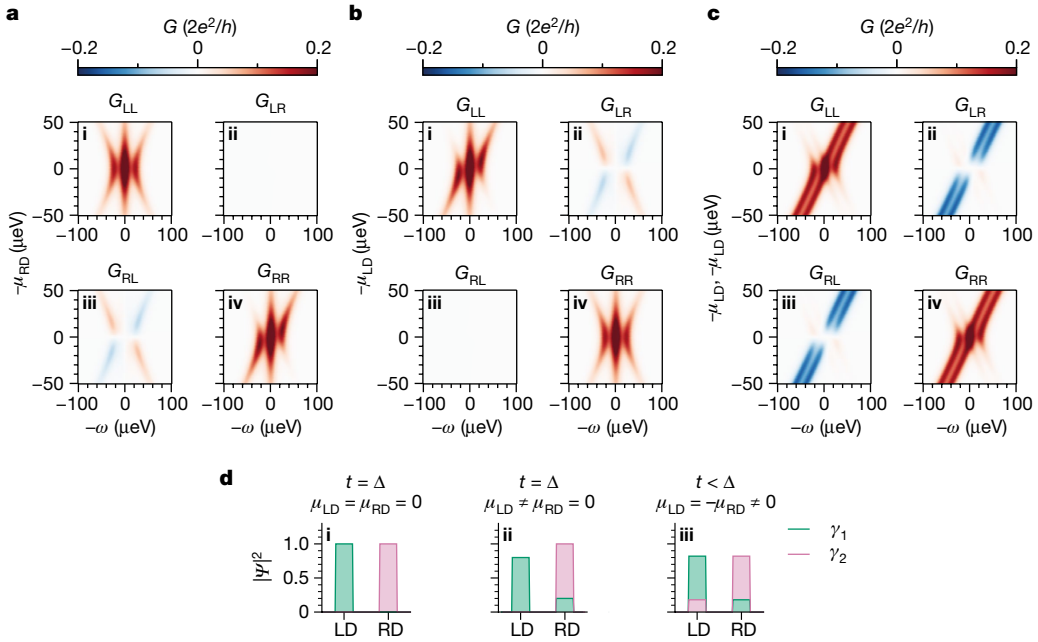


Fig. 4 | Calculated conductance and Majorana localization. a, Numerically calculated G as a function of energy ω and μ_{RD} at the $t = \Delta$ sweet spot. **b**, Numerically calculated G as a function of energy ω and μ_{LD} at the $t = \Delta$ sweet spot. **c**, Numerically calculated G as a function of energy ω and μ_{RD} and μ_{LD} along the diagonal corresponding to $\mu_{LD} = \mu_{RD}$ at $t = \Delta$. All of the numerical curves use the same value of t, Δ, Γ_L and Γ_R as those in Fig. 3. **d**, Illustrations of the localization of two zero-energy solutions for the following set of parameters: $t = \Delta, \mu_{LD} = \mu_{RD} = 0$ (i), $t = \Delta, \mu_{RD} = 0, \mu_{LD} > 0$ (ii) and $t < \Delta, \mu_{LD} = -\mu_{RD} = \sqrt{\Delta^2 - t^2}$ (iii).

of the QD levels deviates from charge degeneracy[3]. We focus on the ↑↑ spin configuration because it exhibits higher t and Δ values when they are equal (see Extended Data Fig. 4). Figure 3a shows the charge-stability diagram measured through I_R under fixed $V_L = 0$ and $V_R = 10$ μV. No level repulsion is visible, indicating $t \approx \Delta$. Figure 3b, i shows the excitation spectrum when both dots are at charge degeneracy. The spectra on both sides show zero-bias peaks accompanied by two side peaks. The values of t and Δ can be read directly from the position of the side peaks, which correspond to the antibonding excited states at energy $2t = 2\Delta \approx 25$ μeV. The height of the observed zero-bias peaks is 0.3 to $0.4 \times 2e^2/h$, probably because of a combination of tunnel broadening and finite electron temperature (Extended Data Fig. 2). Figure 3b, ii shows the spectrum when the right QD is moved away from charge degeneracy while μ_{LD} is kept at 0. The zero-bias peaks persist on both sides of the device, as expected for a PMM state. By contrast, tuning both dots away from charge degeneracy, shown in Fig. 3b, iii, splits the zero-bias peaks.

In Fig. 3c,d, we show the evolution of the spectrum when varying V_{RD} and V_{LD}, respectively. The vertical feature appearing in both G_{LL} and G_{RR} shows correlated zero-bias peaks in both QDs, which persist when one QD potential departs from zero. This crucial observation demonstrates the robustness of PMM states against local perturbations. The excited states disperse, in agreement with the theoretical predictions[3]. Nonlocal conductance, on the other hand, reflects the local charge character of a bound state on the side where current is measured[28–30]. Near-zero values of G_{LR} in panel c and G_{RL} in panel d are consistent with the prediction that the PMM mode on the unperturbed side remains an equal superposition of an electron and a hole, and therefore chargeless.

Finally, when varying the chemical potential of both dots simultaneously (panel e), we see that the zero-bias peaks split away from zero energy. This splitting is not linear, in contrast to the case when $\Delta \neq t$ (see Extended Data Fig. 5). The profile of the peak splitting is consistent with the predicted quadratic protection of PMM states against chemical potential fluctuations[3]. This quadratic protection is expected to develop into topological protection in a long-enough Kitaev chain[2].

Discussion

To facilitate comparison with data, we develop a transport model (see Methods) and plot in Fig. 4a–c the calculated conductance matrices as functions of excitation energy, ω, versus μ_{RD} (panel a), μ_{LD} (panel b) and $\mu \equiv \mu_{LD} = \mu_{RD}$ (panel c). These conditions are an idealization of those in Fig. 3 (a more realistic simulation of the experimental conditions is presented in Extended Data Fig. 6). The numerical simulations capture the main features appearing in the experiments discussed above.

Particle–hole symmetry ensures that zero-energy excitations in this system always come in pairs. These excitations can extend over both QDs or be confined to one of them. In Fig. 4d, we show the calculated spatial extent of the zero-energy excitations for three scenarios. The first, in Fig. 4d, i, illustrates Fig. 3b, i and shows that the sweet-spot zero-energy solutions are two PMM states, each localized on a different QD. The second scenario, Fig. 4d, ii, illustrating Fig. 3b, ii, is varying μ_{LD} while keeping $\mu_{RD} = 0$. This causes some of the wavefunction localized on the perturbed left side, γ_1, to leak into the right QD. Because the right-side γ_2 excitation has no weight on the left, it does not respond to this perturbation and remains fully localized on the right QD. As the theory confirms[3], it stays a zero-energy PMM state. Because Majorana excitations always come in pairs, the excitation on the left QD must also remain at zero energy. This provides an intuitive understanding of the remarkable stability of the zero-energy modes at the sweet spot in Fig. 3c,d when moving the chemical potentials of one of the QDs away from zero. Finally, zero-energy solutions can be found away from the sweet spot, $t \neq \Delta$, as illustrated in Fig. 4d, iii. These zero-energy states are only found when both QDs are off-resonance and none of them are localized Majorana states, extending over both QDs and exhibiting no gate stability. Measurements under these conditions are shown in Extended Data Fig. 5, in which zero-energy states can be found in a variety of gate settings (panels a, c therein).

Conclusion

In summary, we realize a minimal Kitaev chain in which two QDs in an InSb nanowire are separated by a hybrid semiconducting–superconducting segment. Compared with past works, our approach solves three challenges: strong hybridization of QDs through CAR, simultaneous coupling of two single spins through both ECT and CAR, and continuous tuning of the coupling amplitudes. This is made possible by the two QDs as well as the middle Andreev bound state mediating their couplings all being discrete, gate-tunable quantum states. The result is the creation of a new type of nonlocal state that hosts Majorana-type excitations at a fine-tuned sweet spot. The zero-bias peaks at this spot are robust against variations of the chemical potential of one QD and quadratically protected against simultaneous perturbations of both. This discrete and tunable way of assembling Kitaev chains shows good agreement between theory and experiment by avoiding the most concerning problems affecting the continuous nanowire experiments: disorder, smooth gate potentials and multi-subband occupation[31]. The QD-S-QD platform discussed here opens up a new frontier to the study of Majorana physics. In the long term, this approach can generate topologically protected Majorana states in longer chains[2]. A shorter-term approach is to use PMM states as an immediate playground to study fundamental non-Abelian statistics, for example, by fusing neighbouring PMM states in a device with two such copies.

Online content

Any methods, additional references, Nature Portfolio reporting summaries, source data, extended data, supplementary information, acknowledgements, peer review information; details of author contributions and competing interests; and statements of data and code availability are available at https://doi.org/10.1038/s41586-022-05585-1.

1. Kitaev, A. Y. Unpaired Majorana fermions in quantum wires. *Phys.-Uspekhi* **44**, 131 (2001).
2. Sau, J. D. & Das Sarma, S. Realizing a robust practical Majorana chain in a quantum-dot-superconductor linear array. *Nat. Commun.* **3**, 964 (2012).
3. Leijnse, M. & Flensberg, K. Parity qubits and poor man's Majorana bound states in double quantum dots. *Phys. Rev. B* **86**, 134528 (2012).
4. Recher, P., Sukhorukov, E. V. & Loss, D. Andreev tunneling, Coulomb blockade, and resonant transport of nonlocal spin-entangled electrons. *Phys. Rev. B* **63**, 165314 (2001).
5. Hofstetter, L., Csonka, S., Nygård, J. & Schönenberger, C. Cooper pair splitter realized in a two-quantum-dot Y-junction. *Nature* **461**, 960–963 (2009).
6. Herrmann, L. G. et al. Carbon nanotubes as Cooper-pair beam splitters. *Phys. Rev. Lett.* **104**, 026801 (2010).
7. Das, A. et al. High-efficiency Cooper pair splitting demonstrated by two-particle conductance resonance and positive noise cross-correlation. *Nat. Commun.* **3**, 1165 (2012).
8. Schindele, J., Baumgartner, A. & Schönenberger, C. Near-unity Cooper pair splitting efficiency. *Phys. Rev. Lett.* **109**, 157002 (2012).
9. Nayak, C., Simon, S. H., Stern, A., Freedman, M. & Das Sarma, S. Non-Abelian anyons and topological quantum computation. *Rev. Mod. Phys.* **80**, 1083–1159 (2008).
10. Kitaev, A. Y. Fault-tolerant quantum computation by anyons. *Ann. Phys.* **303**, 2–30 (2003).
11. Mourik, V. et al. Signatures of Majorana fermions in hybrid superconductor-semiconductor nanowire devices. *Science* **336**, 1003–1007 (2012).
12. Deng, M. T. et al. Majorana bound state in a coupled quantum-dot hybrid-nanowire system. *Science* **354**, 1557–1562 (2016).
13. Fornieri, A. et al. Evidence of topological superconductivity in planar Josephson junctions. *Nature* **569**, 89–92 (2019).
14. Ren, H. et al. Topological superconductivity in a phase-controlled Josephson junction. *Nature* **569**, 93–98 (2019).
15. Vaitiekėnas, S. et al. Flux-induced topological superconductivity in full-shell nanowires. *Science* **367**, eaav3392 (2020).
16. Kells, G., Meidan, D. & Brouwer, P. W. Near-zero-energy end states in topologically trivial spin-orbit coupled superconducting nanowires with a smooth confinement. *Phys. Rev. B* **86**, 100503 (2012).
17. Prada, E., San-Jose, P. & Aguado, R. Transport spectroscopy of NS nanowire junctions with Majorana fermions. *Phys. Rev. B* **86**, 180503 (2012).
18. Pikulin, D. I., Dahlhaus, J. P., Wimmer, M., Schomerus, H. & Beenakker, C. W. J. A zero-voltage conductance peak from weak antilocalization in a Majorana nanowire. *New J. Phys.* **14**, 125011 (2012).
19. Liu, C.-X., Sau, J. D., Stanescu, T. D. & Das Sarma, S. Andreev bound states versus Majorana bound states in quantum dot-nanowire-superconductor hybrid structures: trivial versus topological zero-bias conductance peaks. *Phys. Rev. B* **96**, 075161 (2017).
20. Vuik, A., Nijholt, B., Akhmerov, A. & Wimmer, M. Reproducing topological properties with quasi-Majorana states. *SciPost Phys.* **7**, 061 (2019).
21. Pan, H. & Das Sarma, S. Physical mechanisms for zero-bias conductance peaks in Majorana nanowires. *Phys. Rev. Res.* **2**, 013377 (2020).
22. Wiel, W. Gvd et al. Electron transport through double quantum dots. *Rev. Mod. Phys.* **75**, 1–22 (2003).
23. Choi, M.-S., Bruder, C. & Loss, D. Spin-dependent Josephson current through double quantum dots and measurement of entangled electron states. *Phys. Rev. B* **62**, 13569 (2000).
24. Liu, C.-X., Wang, G., Dvir, T. & Wimmer, M. Tunable superconducting coupling of quantum dots via Andreev bound states in semiconductor-superconductor nanowires. Preprint at https://arxiv.org/abs/2203.00107 (2022).
25. Wang, G. et al. Singlet and triplet Cooper pair splitting in superconducting-semiconducting hybrid nanowires. *Nature* **612**, 448–453 (2022).
26. Bordin, A. et al. Controlled crossed Andreev reflection and elastic co-tunneling mediated by Andreev bound states. Preprint at https://arxiv.org/abs/2212.02274 (2022).
27. Beckmann, D. & Löhneysen, H. V. Experimental evidence for crossed Andreev reflection. *AIP Conf. Proc.* **850**, 875–876 (2006).
28. Gramich, J., Baumgartner, A. & Schönenberger, C. Andreev bound states probed in three-terminal quantum dots. *Phys. Rev. B* **96**, 195418 (2017).
29. Danon, J. et al. Nonlocal conductance spectroscopy of Andreev bound states: symmetry relations and BCS charges. *Phys. Rev. Lett.* **124**, 036801 (2020).
30. Ménard, G. C. et al. Conductance-matrix symmetries of a three-terminal hybrid device. *Phys. Rev. Lett.* **124**, 036802 (2020).
31. Pan, H. & Das Sarma, S. Disorder effects on Majorana zero modes: Kitaev chain versus semiconductor nanowire. *Phys. Rev. B* **103**, 224505 (2021).

Publisher's note Springer Nature remains neutral with regard to jurisdictional claims in published maps and institutional affiliations.

Springer Nature or its licensor (e.g. a society or other partner) holds exclusive rights to this article under a publishing agreement with the author(s) or other rightsholder(s); author self-archiving of the accepted manuscript version of this article is solely governed by the terms of such publishing agreement and applicable law.

© The Author(s), under exclusive licence to Springer Nature Limited 2023

Methods

Device fabrication

The nanowire hybrid devices presented in this work were fabricated on prepatterned substrates, using the shadow-wall lithography technique described in refs. [32,33]. Nanowires were deposited onto the substrates using an optical micromanipulator setup. Eight nanometres of Al was grown at a mix of 15° and 45° angles with respect to the substrate. Subsequently, device A was coated with 2 Å of Pt grown at 30°. No Pt was deposited for device B. Finally, all devices were capped with 20 nm of evaporated AlO_x. Details of the substrate fabrication, the surface treatment of the nanowires, the growth conditions of the superconductor, the thickness calibration of the Pt coating and the ex situ fabrication of the ohmic contacts can be found in ref. [34]. Devices A and B also slightly differ in the length of the hybrid segment: 180 nm for A and 150 nm for B.

Transport measurement and data processing

We have fabricated and measured six devices with similar geometry. Two of them showed strong hybridization of the QD states by means of CAR and ECT. We report on the detailed measurements of device A in the main text and show qualitatively similar measurements from device B in Extended Data Figs. 7 and 8. All measurements on device A were done in a dilution refrigerator with base temperature 7 mK at the cold plate and electron temperature of about 40–50 mK at the sample, measured in a similar setup using an NIS metallic tunnel junction. Unless otherwise mentioned, the measurements on device A were conducted in the presence of a magnetic field of 200 mT approximately oriented along the nanowire axis with a 3° offset. Device B was measured similarly in another dilution refrigerator under $B = 100$ mT along the nanowire with 4° offset.

Figure 1e shows a schematic depiction of the electrical setup used to measure the devices. The middle segment of the InSb nanowire is covered by a thin Al shell, kept grounded throughout the experiment. On each side of the hybrid segment, we connect the N leads to a current-to-voltage converter. The amplifiers on the left and right sides of the device are each biased through a digital-to-analogue converter that applies DC and AC biases. The total series resistance of the voltage source and the current meter is less than 100 Ω for device A and 1.11 kΩ for device B. Voltage outputs of the current meters are read by digital multimeters and lock-in amplifiers. Current amplifier offsets are calibrated using known zero-conductance features when the device is pinched off or in deep Coulomb blockade. When DC voltage V_L is applied, V_R is kept grounded and vice versa. AC excitations are applied on each side of the device with different frequencies (17 Hz on the left and 29 Hz on the right for device A, 19 Hz on the left and 29 Hz on the right for device B) and with amplitudes between 2 and 6 μV RMS. In this manner, we measure the DC currents I_L and I_R and the conductance matrix G in response to applied voltages V_L and V_R on the left and right N leads, respectively. The conductance matrix is corrected for voltage-divider effects (see ref. [35] for details) taking into account the series resistance of sources and meters and in each fridge line (1.85 kΩ for device A and 2.5 kΩ for device B), except for the right panels of Figs. 1h and 2d. There, the left half of the conductance matrix was not measured and correction is not possible. We verify that the series resistance is much smaller than device resistance and the voltage-divider effect is never more than about 10% of the signal.

Characterization of QDs and the hybrid segment

To form the QDs described in the main text, we pinch off the finger gates next to the three ohmic leads, forming two tunnel barriers in each N-S junction. V_{LD} and V_{RD} applied on the middle finger gates on each side accumulate electrons in the QDs. We refer to the associated data repository for the raw gate voltage values used in each measurement. See Extended Data Fig. 1a–f for results of the dot characterizations.

Characterization of the spectrum in the hybrid segment is done using conventional tunnel spectroscopy. In each uncovered InSb segment, we open up the two finger gates next to the N lead and only lower the gate next to the hybrid to define a tunnel barrier. The results of the tunnel spectroscopy are shown in Extended Data Fig. 1g,h and the raw gate voltages are available in the data repository.

Determination of QD spin polarization

Control of the spin orientation of QD levels is done by means of selecting from the even versus odd charge degeneracy points following the method detailed in ref. [36]. At the charge transition between occupancy $2n$ and $2n + 1$ (n being an integer), the electron added to or removed from the QD is polarized to spin-down (↓, lower in energy). The next level available for occupation, at the transition between $2n + 1$ and $2n + 2$ electrons, has the opposite polarization of spin-up (↑, higher in energy). To ensure that the spin polarization is complete, the experiment was conducted with $E_Z \approx 400\ \mu\text{eV} > |eV_L|, |eV_R|$ (see Extended Data Fig. 1 for determination of the spin configuration). In the experimental data, a change in the QD spin orientation is visible as a change in the range of V_{LD} or V_{RD}.

Controlling ECT and CAR through electric gating

Reference[24] describes a theory of mediating CAR and ECT transitions between QDs by means of virtual hopping through an intermediate Andreev bound state. Reference[26] experimentally verifies the applicability of this theory to our device. To summarize the findings here, we consider two QDs both tunnel-coupled to a central Andreev bound state in the hybrid segment of the device. The QDs have excitation energies lower than that of the Andreev bound state and thus transition between them is second order. The wavefunction of an Andreev bound state consists of a superposition of an electron part, u, and a hole part, v. Both theory and experiment conclude that the values of t and Δ depend strongly and differently on u and v. Specifically, CAR involves converting an incoming electron to an outgoing hole and thus depends on the values of u and v jointly as $|uv|^2$. ECT, however, occurs over two parallel channels (electron-to-electron and hole-to-hole) and its coupling strength depends on u and v independently as $|u^2 - v^2|^2$. As the composition of u and v is a function of the chemical potential of the middle Andreev bound state, the CAR-to-ECT ratio is strongly tunable by V_{PG}. We thus look for a range of V_{PG} at which Andreev bound states reside in the hybrid segment, making sure that the energies of these states are high enough so as not to hybridize with the QDs directly (Extended Data Fig. 1). Next we sweep V_{PG} to find the crossover point between t and Δ, as described in the main text.

Further details on the measurement of the coupled QD spectrum

The measurement of the local and nonlocal conductance shown in Fig. 2g was conducted in a series of steps. First, the value of V_{PG} was set and a charge-stability diagram was measured as a function of V_{LD} and V_{RD}. Representative examples of such diagrams are shown in Extended Data Fig. 3. Second, each charge-stability diagram was inspected and the joint charge degeneracy point ($\mu_{LD} = \mu_{RD} = 0$) was selected manually (V^0_{LD}, V^0_{RD}). Last, the values of V_{LD} and V_{RD} were set to those of the joint degeneracy point and the local and nonlocal conductance were measured as a function of V_R.

The continuous transition from $t > \Delta$ to $t < \Delta$ is visible in Fig. 2g through both local and nonlocal conductance. G_{RR} shows that level repulsion splits the zero-energy resonance peaks both when $t > \Delta$ (lower values of V_{PG}) and when $t < \Delta$ (higher values of V_{PG}). The zero-bias peak is restored in the vicinity of $t = \Delta$, in agreement with theoretical predictions[3]. The crossover is also apparent in the sign of G_{LR}, which changes from negative ($t > \Delta$) to positive ($t < \Delta$).

To better visualize the transition between the ECT-dominated and CAR-dominated regimes, we extract V_{PP}, the separation between the

conductance peaks under positive and negative bias voltages, and plot them as a function of V_{PG} in Fig. 2h. When tuning V_{PG}, the peak spacing decreases until the two peaks merge at $V_{PG} \approx 210$ mV. Further increase of V_{PG} leads to increasing V_{PP}. Furthermore, to observe the change in sign of the nonlocal conductance, we follow $\langle G_{LR} \rangle$, the value of G_{LR} averaged over the bias voltage V_R between −100 and 100 μV at a given V_{PG}. We see that $\langle G_{LR} \rangle$ turns from negative to positive at $V_{PG} \approx 210$ mV, in correspondence to a change in the dominant coupling mechanism.

Figure 3c–e presents measurements at which the conductance was measured against applied biases along some paths within the charge-stability diagram (panel a). Before each of these measurements, a charge stability-diagram was measured and inspected, on the basis of which the relevant path in the (V_{LD}, V_{RD}) plane was chosen. Following each bias spectroscopy measurement, another charge-stability diagram was measured and compared with the one taken before to check for potential gate instability. In case of noticeable gate drifts between the two, the measurement was discarded and the process was repeated. The values of μ_{LD} and μ_{RD} required for theoretical curves appearing in panel b were calculated by $\mu_i = \alpha_i(V_i - V_i^0)$, in which i = LD, RD and α_i is the lever arm of the corresponding QD. The discrepancy between the spectra measured with G_{LL} and G_{RR} probably results from gate instability, as they were not measured simultaneously. Finite remaining G_{LR} in panel c and G_{RL} in panel d probably result from small deviations of μ_{LD} and μ_{RD} from zero during these measurements.

Model of the phase diagrams in Fig. 1f

To calculate the ground state phase diagram in Fig. 1f, we write the Hamiltonian in the many-body picture, with the four basis states being $|00\rangle$, $|11\rangle$, $|10\rangle$ and $|01\rangle$:

$$H_{mb} = \begin{pmatrix} 0 & \Delta & 0 & 0 \\ \Delta & \varepsilon_L + \varepsilon_R & 0 & 0 \\ 0 & 0 & \varepsilon_L & t \\ 0 & 0 & t & \varepsilon_R \end{pmatrix} \tag{2}$$

in block-diagonalized form. The two 2 × 2 matrices yield the energy eigenvalues separately for the even and odd subspaces:

$$E_{o,\pm} = \frac{\varepsilon_L + \varepsilon_R}{2} \pm \sqrt{\left(\frac{\varepsilon_L - \varepsilon_R}{2}\right)^2 + t^2} \tag{3}$$

$$E_{e,\pm} = \frac{\varepsilon_L + \varepsilon_R}{2} \pm \sqrt{\left(\frac{\varepsilon_L + \varepsilon_R}{2}\right)^2 + \Delta^2} \tag{4}$$

The ground state phase transition occurs at the boundary $E_{o,-} = E_{e,-}$. This is equivalent to

$$\varepsilon_L \varepsilon_R = t^2 - \Delta^2 \tag{5}$$

Transport model in Figs. 3 and 4

We describe in this section the model Hamiltonian of the minimal Kitaev chain and the method we use for calculating the differential conductance matrices when the Kitaev chain is tunnel-coupled to two external N leads.

The effective Bogoliubov-de-Gennes Hamiltonian of the double-QD system is

$$\begin{aligned} H &= \varepsilon_L c_L^\dagger c_L + \varepsilon_R c_R^\dagger c_R + t c_L^\dagger c_R + t c_R^\dagger c_L + \Delta c_L c_R + \Delta c_R^\dagger c_L^\dagger \\ &= \frac{1}{2}\Psi^\dagger \begin{pmatrix} \varepsilon_L & t & 0 & -\Delta \\ t & \varepsilon_R & \Delta & 0 \\ 0 & \Delta & -\varepsilon_L & -t \\ -\Delta & 0 & -t & -\varepsilon_R \end{pmatrix} \Psi, \end{aligned} \tag{6}$$

in which $\Psi = (c_L, c_R, c_L^\dagger, c_R^\dagger)^\top$ is the Nambu spinor, $\varepsilon_{L/R}$ is the level energy in dot-L/R relative to the superconducting Fermi surface and t and Δ are the ECT and CAR amplitudes. Here we assume t and Δ to be real without loss of generality[3]. The presence of both t and Δ in this Hamiltonian implies breaking spin conservation during QD-QD tunnelling by means of either spin–orbit coupling (as done in the present experiment) or non-collinear magnetization between the two QDs (as proposed in ref. [3]). Without one of them, equal-spin QDs cannot recombine into a Cooper pair, leading to vanishing Δ, whereas opposite-spin QDs cannot support finite t. The exact values of t and Δ depend on the spin–orbit coupling strength and we refer to ref. [24] for a detailed discussion.

To calculate the differential conductance for the double-QD system, we use the S-matrix method[37]. In the wide-band limit, the S matrix is

$$S(\omega) = \begin{pmatrix} s_{ee} & s_{eh} \\ s_{he} & s_{hh} \end{pmatrix} = 1 - iW^\dagger \left(\omega - H + \frac{1}{2} iWW^\dagger\right)^{-1} W, \tag{7}$$

in which $W = \mathrm{diag}\{\sqrt{\Gamma_L}, \sqrt{\Gamma_R}, -\sqrt{\Gamma_L}, -\sqrt{\Gamma_R}\}$ is the tunnel matrix, with Γ_α being the tunnel coupling strength between dot-α and lead-α. The zero-temperature differential conductance is given by

$$G^0_{\alpha\beta}(\omega) = \mathrm{d}I_\alpha/\mathrm{d}V_\beta = \frac{e^2}{h}\left(\delta_{\alpha\beta} - \left|s^{\alpha\beta}_{ee}(\omega)\right|^2 + \left|s^{\alpha\beta}_{he}(\omega)\right|^2\right), \tag{8}$$

in which α, β = L/R. The finite-temperature effect is included by a convolution between the zero-temperature conductance and the derivative of Fermi–Dirac distribution, that is,

$$G^T(\omega) = \int \mathrm{d}E \frac{G^0(E)}{4k_B T \cosh^2[(E-\omega)/2k_B T]}. \tag{9}$$

The theoretical model presented above uses five input parameters to calculate the conductance matrix under given μ_{LD}, μ_{RD}, V_L and V_R. The input parameters are: t, Δ, Γ_L, Γ_R and T. To choose the parameters in Fig. 3b, i, we fix the temperature to the measured value T = 45 mK and make the simplification $t = \Delta$ and $\Gamma \equiv \Gamma_L = \Gamma_R$. This results in only two free parameters t and Γ, which we manually choose and compare with data. Although oversimplified, this approach allows us to obtain a reasonable match between theory and data taken at $\mu_{LD} = \mu_{RD} = 0$ without the risk of overfitting. To obtain the other numerical curves shown in Fig. 3, we keep the same choice of t and Γ and vary μ_{LD}, μ_{RD}, V_L and V_R along various paths in the parameter space. Similarly, to model the data shown in Extended Data Fig. 5, we keep T = 45 mK and Γ the same as in Fig. 3. The free parameters to be chosen are thus t and Δ. The theory panels are obtained with the same t and Δ, and only μ_{LD}, μ_{RD}, V_L, and V_R are varied in accordance with the experimental conditions.

Finally, we comment on the physical meaning of the theory predictions in Fig. 4a–c. Tuning μ_{RD} leads to symmetric G_{LL} and asymmetric G_{RR}, as well as zero G_{LR} and finite G_{RL} with an alternating pattern of positive and negative values. As discussed in the main text, these features, also seen in the measurements, stem from the local charge of the system: keeping $\mu_{LD} = 0$ maintains zero local charge on the left dot, whereas varying μ_{RD} creates finite local charge on the right dot. The complementary picture appears when varying μ_{LD} in panel b. The asymmetry in both G_{LL} and G_{RR} and the negative nonlocal conductance when tuning simultaneously $\mu_{LD} = \mu_{RD}$ are also captured in the numerical simulation in panel c. We note that, although there is a qualitative agreement between the features in Figs. 3e and 4c, they were obtained under nominally different conditions. As mentioned, the theoretical curve follows $\mu_{LD} = \mu_{RD}$, whereas the experimental curve was taken through a path along which V_{LD} changed twice as much as V_{RD}, although the lever arms of both QDs are similar. In Fig. 4c, we calculate the conductance along a path reproducing the experimental conditions. We speculate that the discrepancy between Fig. 3e and Fig. 4c could arise from some hybridization between the left QD and the superconducting segment as seen in Extended Data Fig. 1.

Data availability

Raw data presented in this work, the data processing/plotting code and code used for the theory calculations are available at https://doi.org/10.5281/zenodo.6594169.

32. Heedt, S. et al. Shadow-wall lithography of ballistic superconductor–semiconductor quantum devices. *Nat. Commun.* **12**, 4914 (2021).
33. Borsoi, F. et al. Single-shot fabrication of semiconducting–superconducting nanowire devices. *Adv. Funct. Mater.* **31**, 2102388 (2021).
34. Mazur, G. P. et al. Spin-mixing enhanced proximity effect in aluminum-based superconductor–semiconductor hybrids. *Adv. Mater.* **34**, 2202034 (2022).
35. Martinez, E. A. et al. Measurement circuit effects in three-terminal electrical transport measurements. Preprint at https://doi.org/10.48550/arXiv.2104.02671 (2021).
36. Hanson, R., Kouwenhoven, L. P., Petta, J. R., Tarucha, S. & Vandersypen, L. M. K. Spins in few-electron quantum dots. *Rev. Mod. Phys.* **79**, 1217–1265 (2007).
37. Datta, S. *Quantum Transport: Atom to Transistor* (Cambridge Univ. Press, 2005).
38. Kouwenhoven, L. P., Austing, D. G. & Tarucha, S. Few-electron quantum dots. *Rep. Prog. Phys.* **64**, 701–736 (2001).

Acknowledgements This work has been supported by the Dutch Organisation for Scientific Research (NWO), a subsidy for Top Consortia for Knowledge and Innovation (TKI toeslag), Microsoft Corporation Station Q and support from the European Union's Horizon 2020 research and innovation programme under grant agreement no. 828948, project AndQC. We thank G. de Lange, S. Goswami, D. Xu, D. Loss and J. Klinovaja for helpful discussions.

Author contributions G.W., G.P.M., N.v.L., A.B., J.-Y.W., D.v.D. and F.Z. fabricated the devices. G.W., T.D., S.L.D.t.H., A.B. and X.L. performed the electrical measurements. T.D. and G.W. designed the experiment with inputs from F.K.M. and analysed the data. G.W., T.D. and L.P.K. prepared the manuscript with input from all authors. T.D. and L.P.K. supervised the project. C.-X.L. developed the theoretical model and performed numerical simulations with input from G.W., T.D. and M.W. S.G., G.B. and E.P.A.M.B. performed InSb nanowire growth.

Competing interests The authors declare no competing interests.

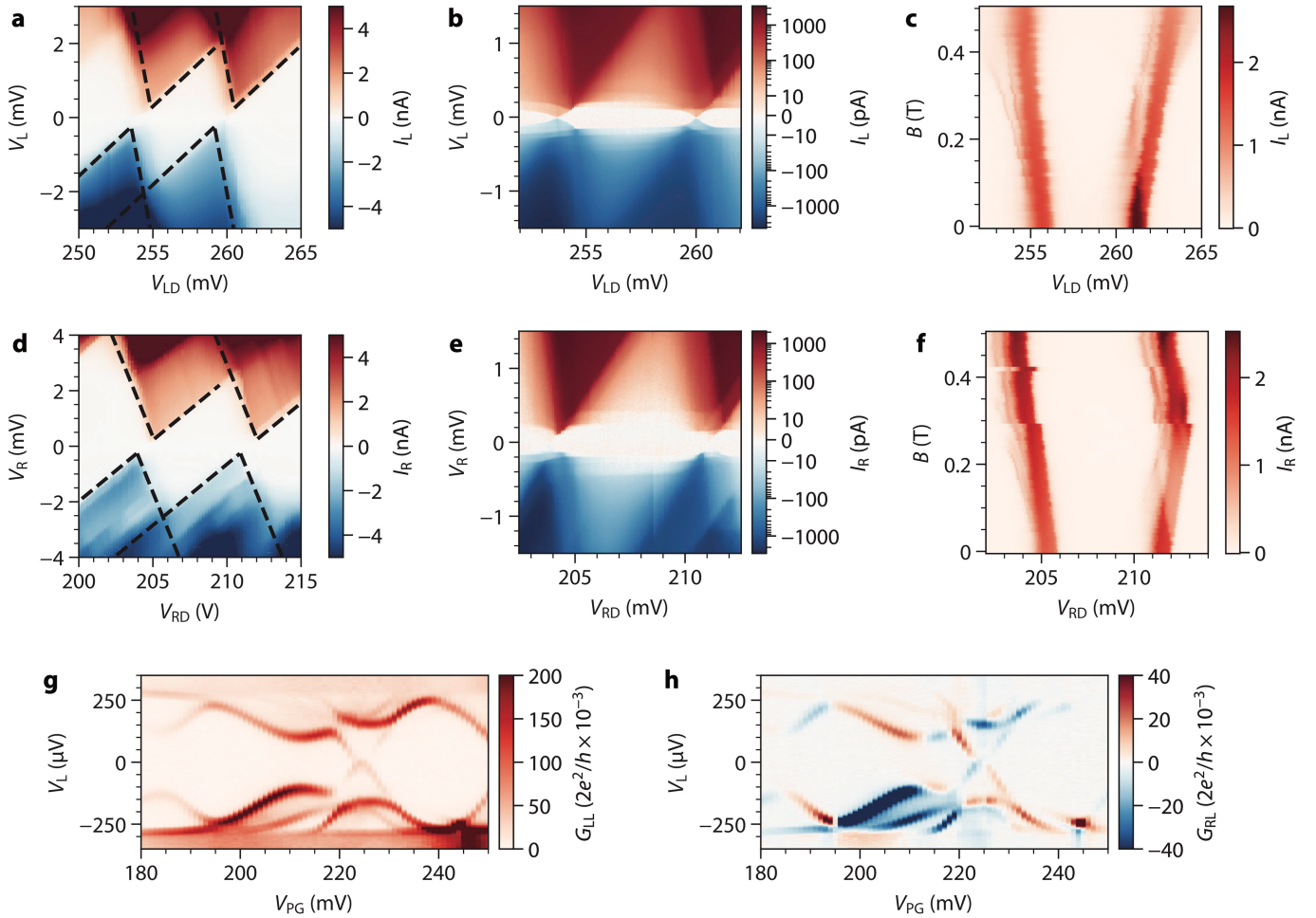
Additional information

Supplementary information The online version contains supplementary material available at https://doi.org/10.1038/s41586-022-05585-1.

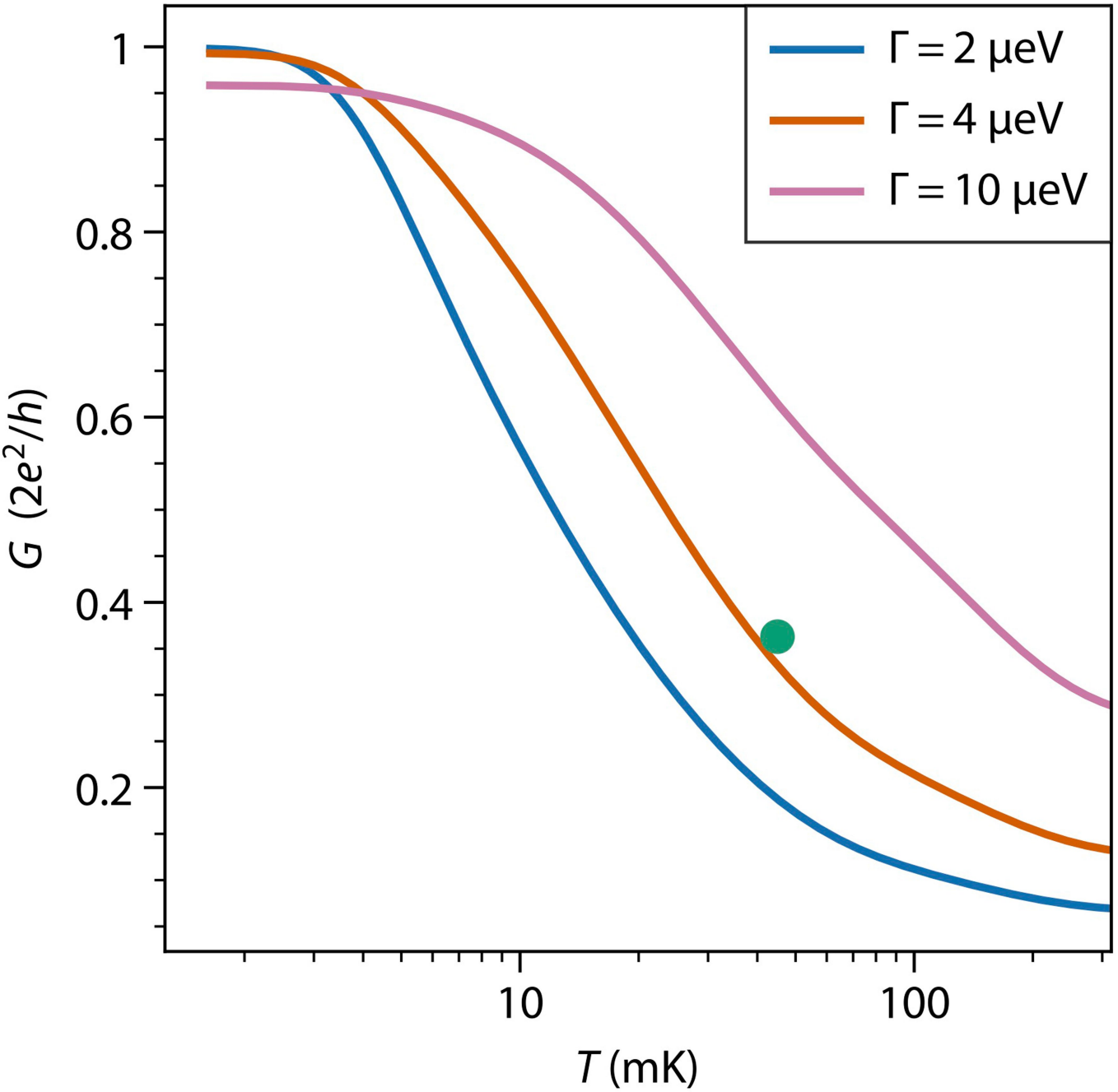
Correspondence and requests for materials should be addressed to Tom Dvir or Leo P. Kouwenhoven.

Peer review information *Nature* thanks Sumanta Tewari, Hongqi Xu and the other, anonymous, reviewer(s) for their contribution to the peer review of this work. Peer reviewer reports are available.

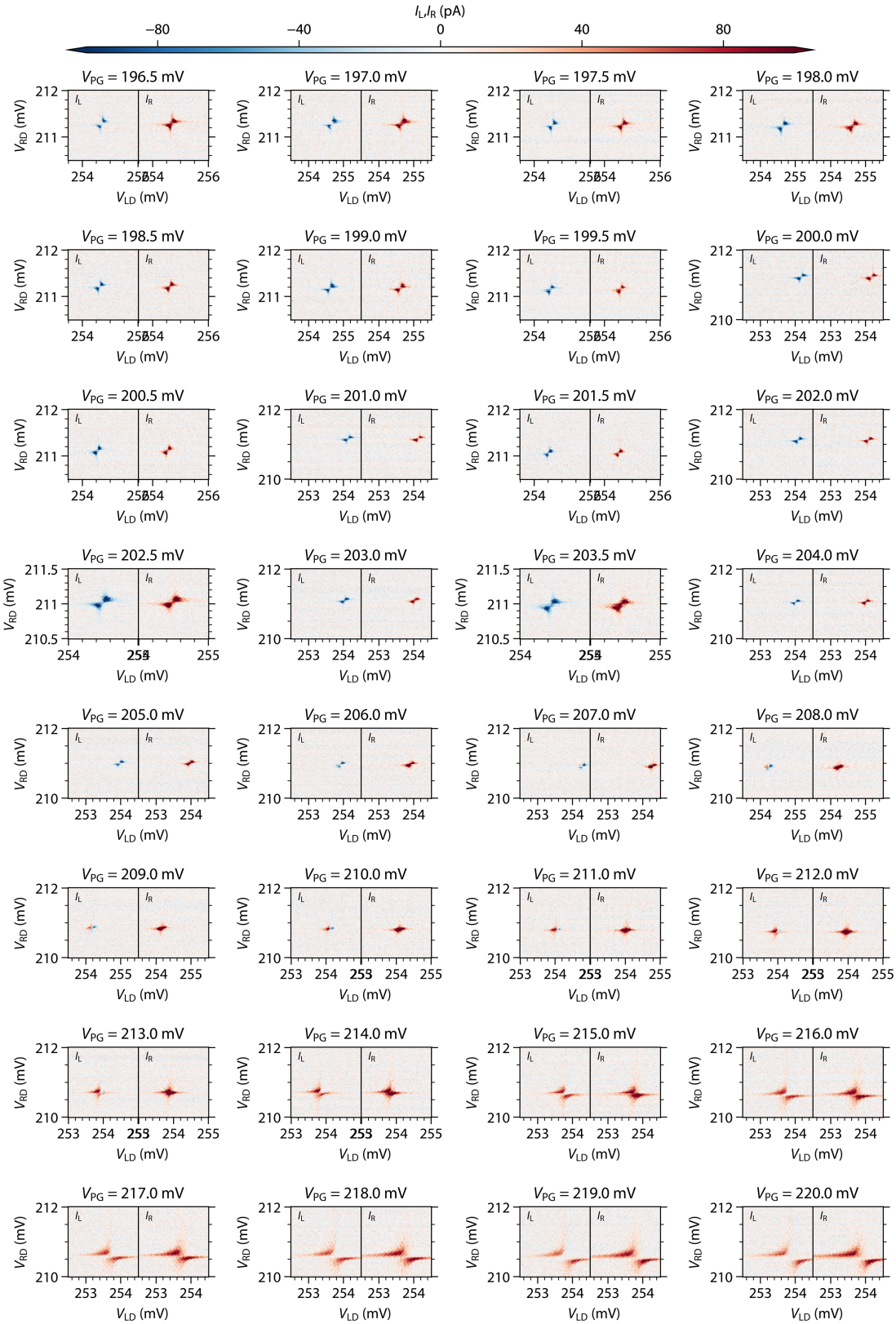
Reprints and permissions information is available at http://www.nature.com/reprints.



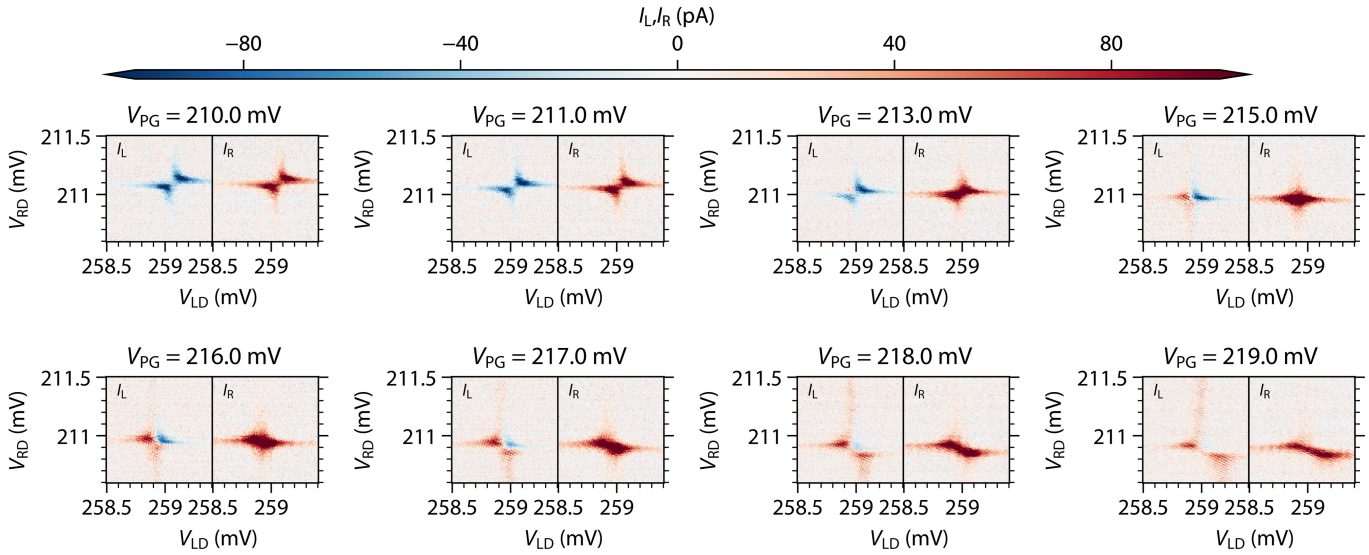
Extended Data Fig. 1 | Characterization of the QDs. a, Coulomb blockade diamonds of the left QD when the right QD is off-resonance. I_L is measured as a function of V_L and V_{LD}. The data are overlaid with a constant interaction model[38] with 1.8-meV charging energy and gate lever arm of 0.32. **b**, A high-resolution scan of **a** with a symmetric logarithmic colour scale to show the presence of a small amount of Andreev current at sub-gap energies. This is because of the left QD being weakly proximitized by local Andreev coupling to Al. **c**, Field dependence of the Coulomb resonances. I_L is measured as a function of V_{LD} and B with a constant $V_L = 600$ μV. The resonances of opposite spin polarization evolve in opposite directions with a g-factor of about 35, translating to Zeeman energy of 400 μeV at $B = 200$ mT. **d**–**f**, Characterization of the right QD, as described in the captions of panels **a**–**c**. Overlaid model in **d** has charging energy 2.3 meV and gate lever arm of 0.33. No sub-gap transport is detectable in **e**. B dispersion in **f** corresponds to $g = 40$. **g**,**h**, Bias spectroscopy results of the proximitized InSb segment under the thin Al/Pt film. I_L and I_R are measured as a function of V_L and V_{PG}. G_{LL} and G_{RL} are obtained by taking the numerical derivative of I_L and I_R along the bias direction after applying a Savitzky–Golay filter of window length 15 and order 1. The sub-gap spectrum shows discrete, gate-dispersing Andreev bound states. The presence of nonlocal conductance correlated with the sub-gap states shows that these Andreev bound states extend throughout the entire hybrid segment, coupling to both left and right N leads[30]. Parts of this dataset are also presented in ref. [34]. (Reproduced under the terms of the CC-BY Creative Commons Attribution 4.0 International license (https://creativecommons.org/licenses/by/4.0). Copyright 2022, The Authors, published by Wiley-VCH.).



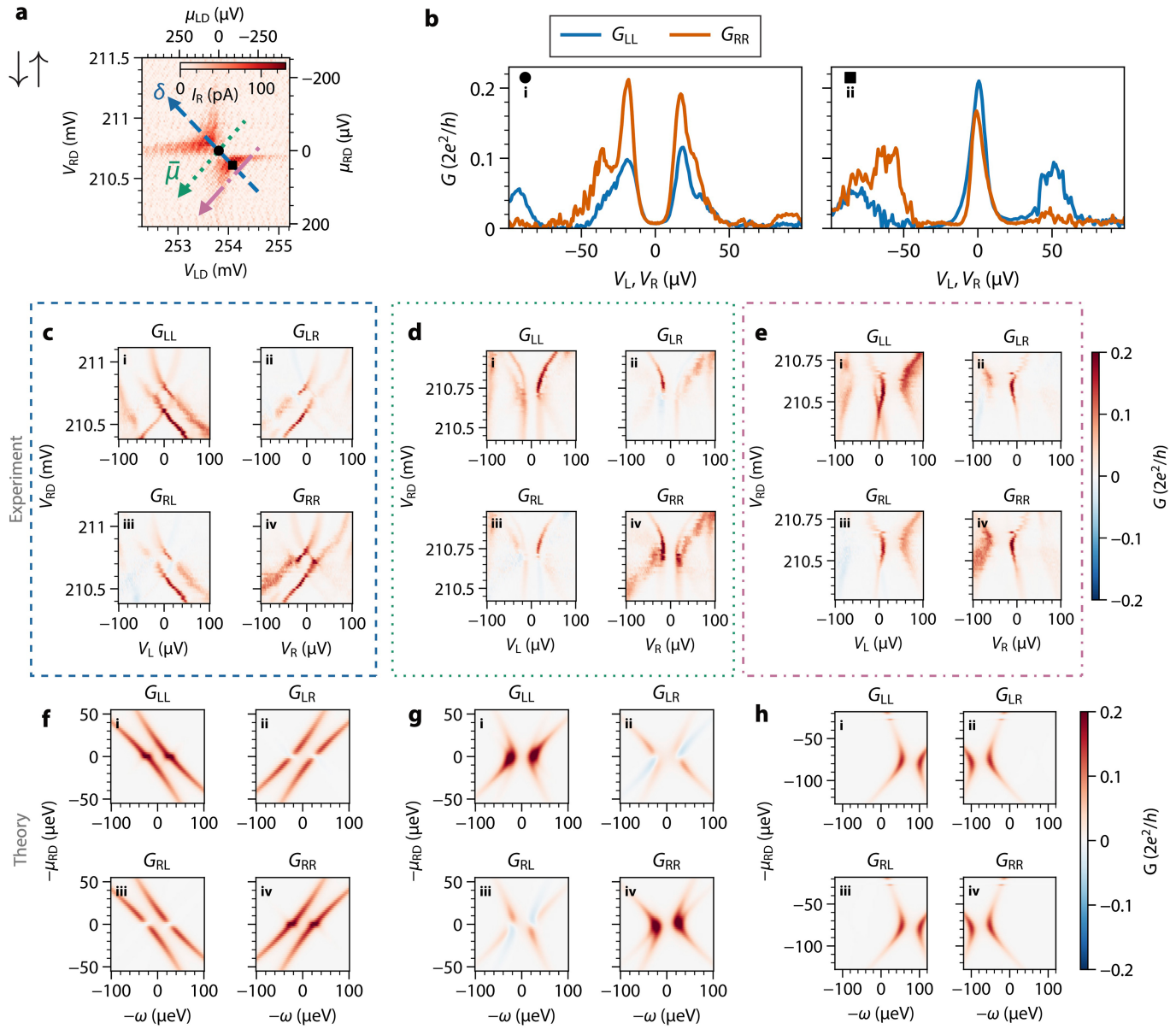
Extended Data Fig. 2 | Theoretical temperature dependence of the height of Majorana zero-bias conductance peaks. The height of the Majorana zero-bias peaks is only quantized to $2e^2/h$ at zero temperature. At finite electron temperature T, the peak height is generally lower, with the exact value depending on T and tunnel broadening Γ_L and Γ_R owing to coupling between QDs and N leads. The local zero-bias conductance G_{LL} at the sweet spot ($t = \Delta$ and $\mu_{LD} = \mu_{RD} = 0$) is calculated and shown in this plot as a function of T, using the parameters presented in Fig. 3: $t = \Delta = 12$ μeV. Three curves are calculated assuming three different values of tunnel coupling $\Gamma = \Gamma_L = \Gamma_R$. The orange curve assumes a Γ value that matches the experimentally observed peak width (both of the zero-bias peaks and of generic QD resonant peaks at other conductance features), showing that conductance approaching quantization would only be realized at electron temperatures <5 mK, unattainable in our dilution refrigerator. The blue curve, calculated with lower Γ = 2 μeV, shows even lower conductance. Increasing Γ would not lead to conductance quantization either, as the zero-bias peaks would merge with the conductance peaks arising from the excited states (pink curve). The green dot marks the experimentally measured electron temperature and peak height (averaged between the values obtained on the left and right leads).



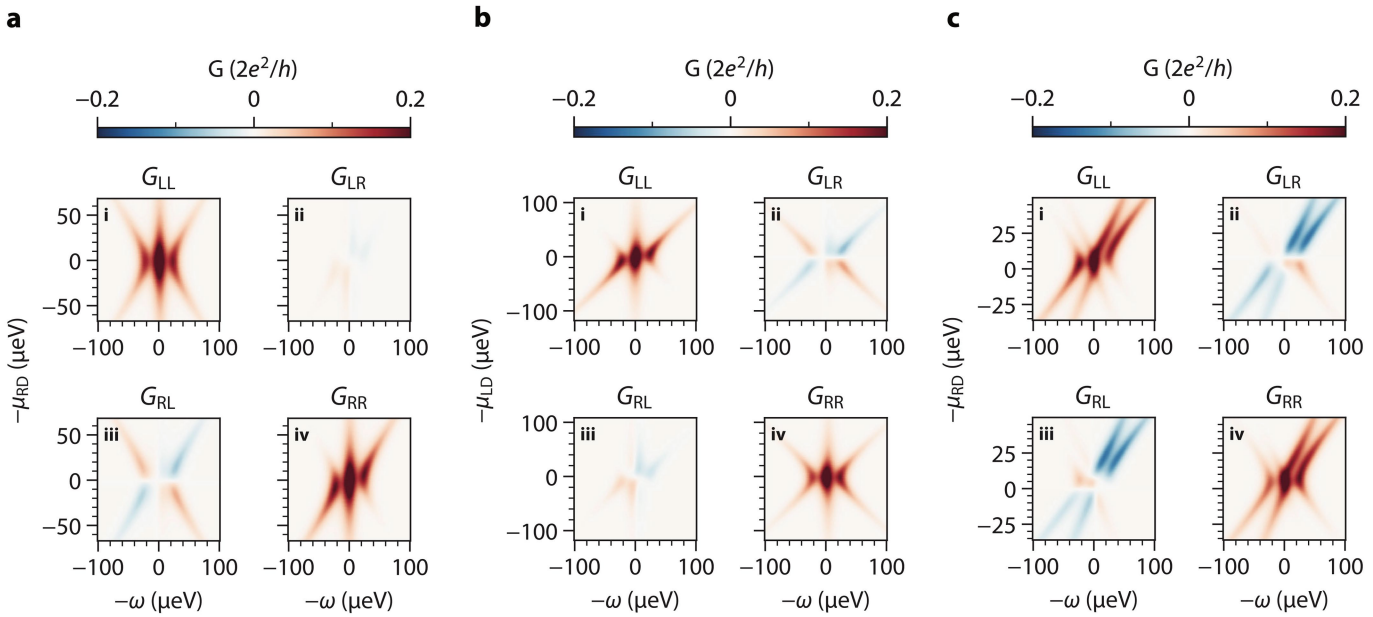
Extended Data Fig. 3 | Evolution of the charge-stability diagram for the ↓↑ spin configuration. Each panel shows I_L (nonlocal) and I_R (local) as functions of V_{LD} and V_{RD} measured under fixed biases $V_L = 0$ and $V_R = 10$ μV. V_{PG} is tuned from 196.5 mV, showing signatures of the $t > \Delta$ regime in both local and nonlocal currents, to 220 mV, featuring the opposite $t < \Delta$ regime.



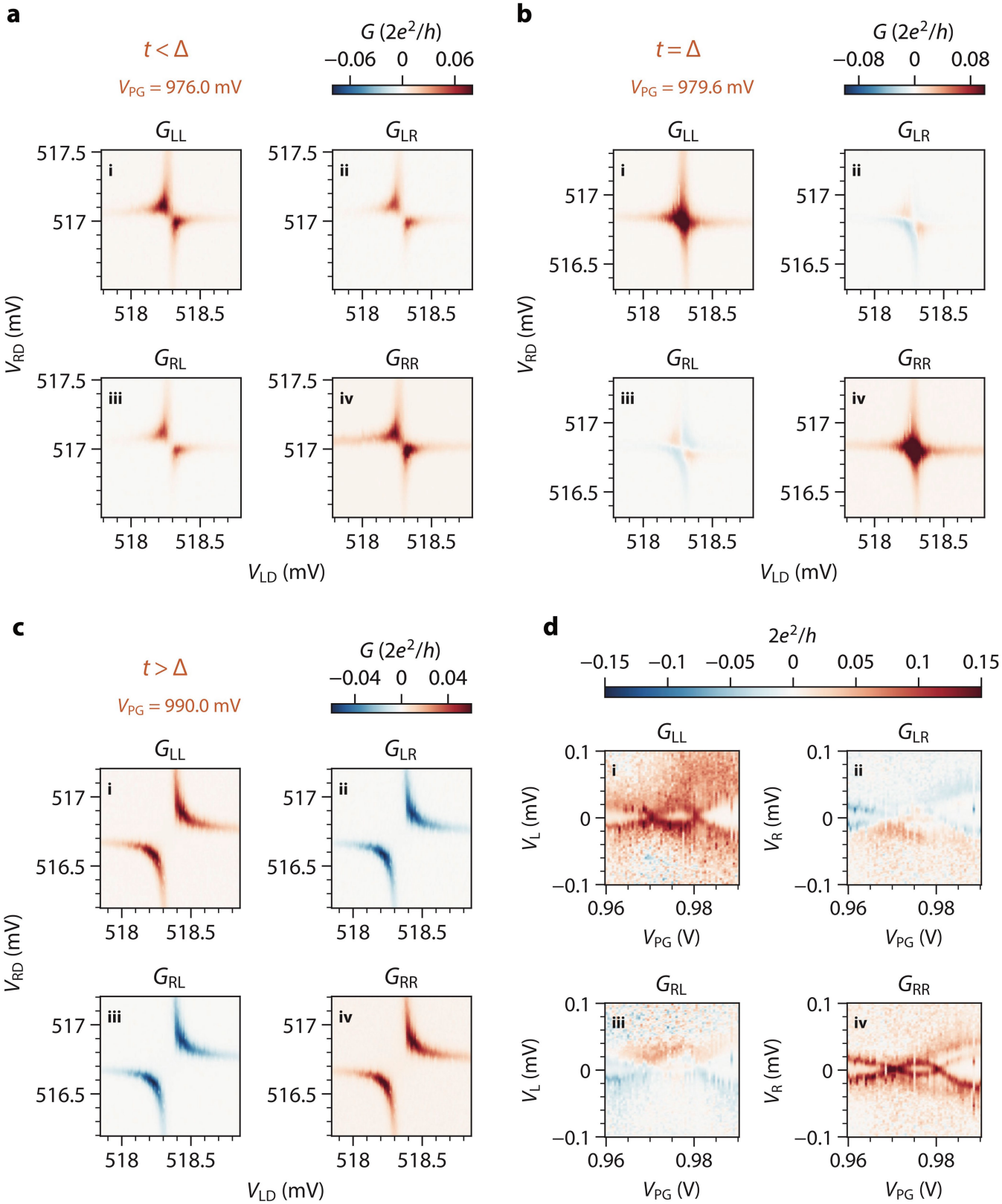
Extended Data Fig. 4 | Evolution of the charge-stability diagram for the ↑↑ spin configuration. Each panel shows I_L (nonlocal) and I_R (local) as functions of V_{LD} and V_{RD} measured under fixed biases $V_L = 0$ and $V_R = 10$ μV. V_{PG} is tuned from 210 mV, showing signatures of the $t > \Delta$ regime in both local and nonlocal currents, to 219 mV, featuring the opposite $t < \Delta$ regime.



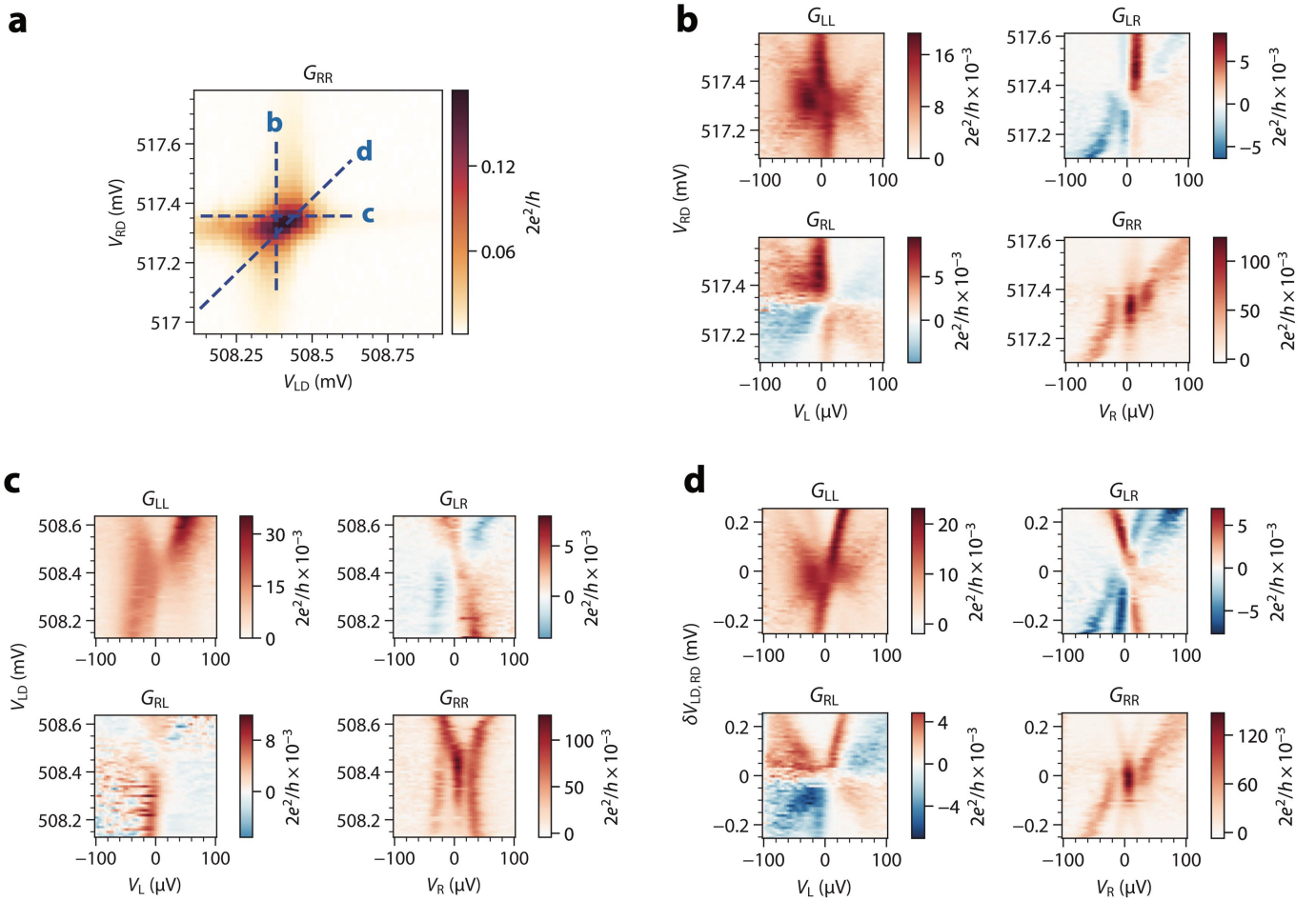
Extended Data Fig. 5 | Conductance spectroscopy when $t < \Delta$. **a**, I_R versus μ_{LD} and μ_{RD} with $V_R = 10$ μV. The evolution of the spectrum with the chemical potential is taken along the dashed, dashed-dotted and dotted lines in panels **b**, **c** and **d**, respectively. Data taken at the ↓↑ spin configuration with fixed $V_{PG} = 218$ mV. **b**, Local conductance spectroscopy taken at gate setpoints marked by corresponding symbols in panel **a**. **c**, Conductance matrix as a function of bias and V_{LD}, taken along the dashed blue line in panel **a**, that is, varying the detuning between the QDs $\delta = (\mu_{LD} - \mu_{RD})/2$ while keeping the average chemical potential $\bar{\mu} = (\mu_{LD} + \mu_{RD})/2$ close to 0. **d**, Conductance matrix as a function of bias and V_{LD}, taken along the dotted green line in panel **a**, keeping the detuning between the QDs around 0. **e**, Conductance matrix as a function of bias and V_{LD}, taken along the dashed-dotted pink line in panel **a**, keeping roughly constant non-zero detuning between the QDs. **f**–**h**, Numerically calculated G as a function of energy ω and μ_{LD} and μ_{RD} along the paths shown in panel **a**. All of the numerical curves assume the same parameters as those in Fig. 3, except with $\Delta = 23$ μeV and $t = 6$ μeV.



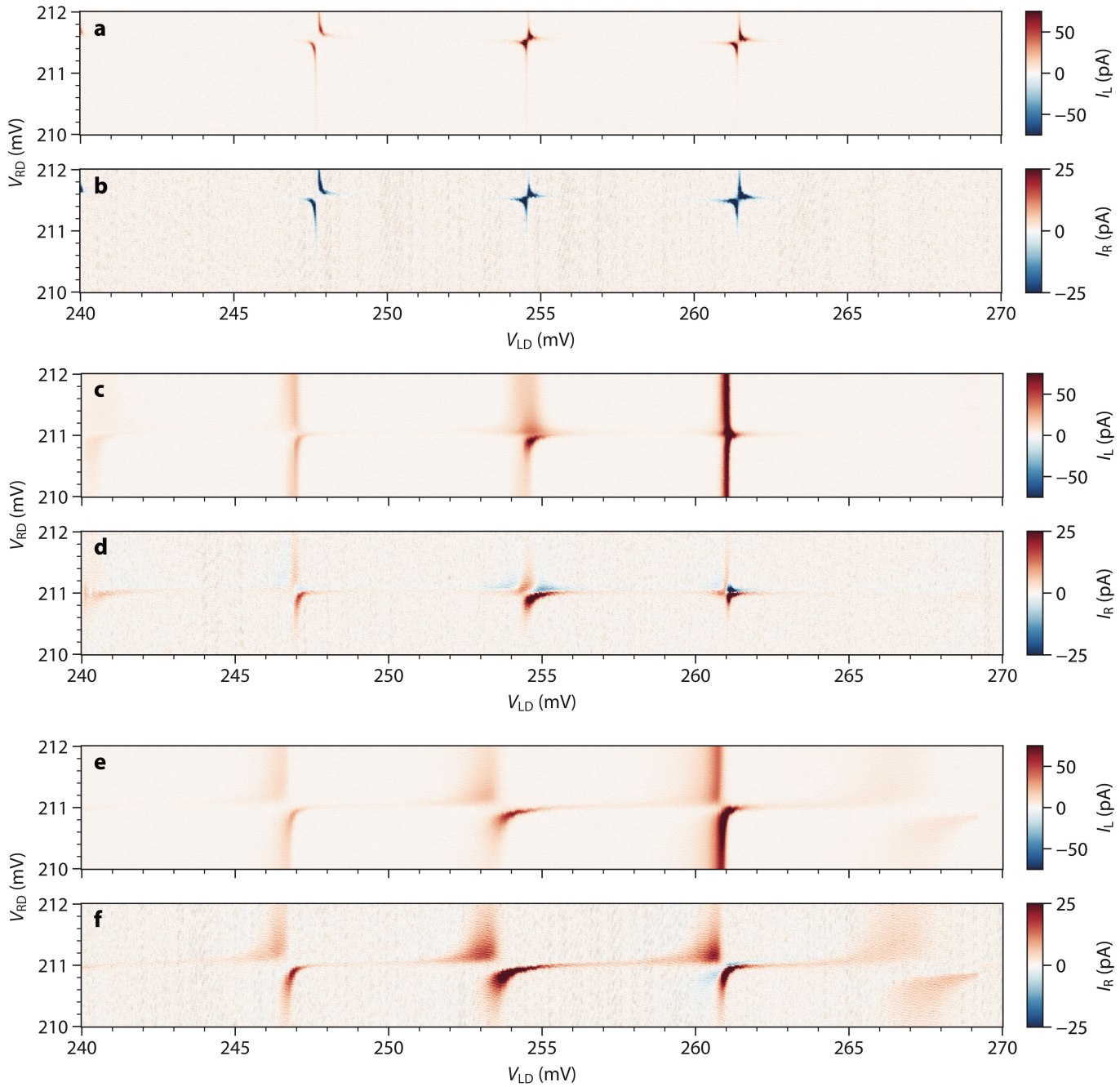
Extended Data Fig. 6 | Calculated conductance matrices at the $t = \Delta$ sweet spot. a, Numerically calculated G as a function of energy ω and μ_{LD} and μ_{RD} along the path shown in Fig. 3c. The presence of finite G_{LR} and asymmetric G_{RL} result from a slight deviation from the $\mu_{LD} = 0$ condition, which is depicted in Fig. 4a. These features appear in the experimental data shown in Fig. 3c. **b**, Numerically calculated G as a function of energy ω and μ_{LD} and μ_{RD} along the path shown in Fig. 3d. The presence of finite G_{RL} and asymmetric G_{LR} result from a slight deviation from the $\mu_{RD} = 0$ condition, which is depicted in Fig. 4b. These features appear in the experimental data shown in Fig. 3d. **c**, Numerically calculated G as a function of energy ω and μ_{LD} and μ_{RD} along the path shown in Fig. 3e. Because the path does not obey $\mu_{LD} = \mu_{RD}$, the calculated spectral lines do not follow parallel trajectories, in slight disagreement with the experimental data. The conversion from V_{LD} and V_{RD} to μ_{LD} and μ_{RD} is carried out as explained in Methods with the measured lever arms of both QDs.



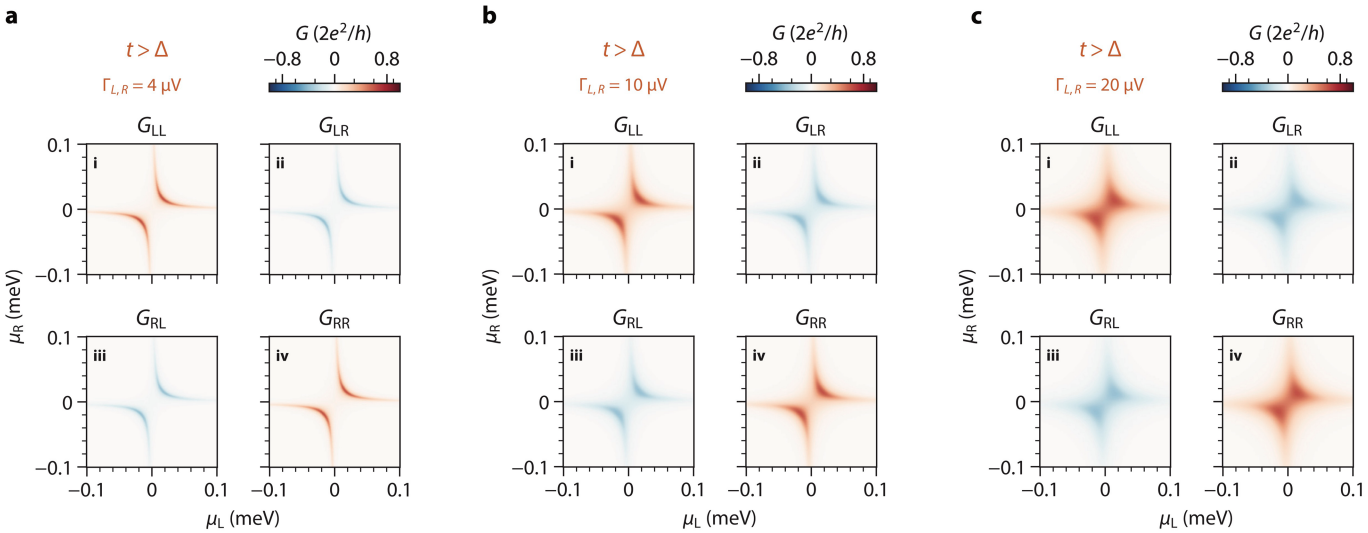
Extended Data Fig. 7 | Reproduction of the main results with device B. a–**c**, Conductance matrices measured at V_{PG} = (976, 979.6 and 990 mV, respectively. **d**, Conductance matrix as a function of V_L and V_R and V_{PG} while keeping $\mu_{LD} \approx \mu_{RD} \approx 0$. This device shows two continuous crossovers from $t > \Delta$ to $t < \Delta$ and again to $t > \Delta$.



Extended Data Fig. 8 | Device B spectrum versus gates. a, Charge-stability diagram measured through G_{RR} of another $t = \Delta$ sweet spot of device B, at V_{PG} = 993 mV. Dashed lines mark the gate voltage paths along which the corresponding panels are taken. **b**–**d**, Conductance matrices when varying V_{RD} (**b**), V_{LD} (**c**) and the two gates simultaneously (**d**), similar to Fig. 3. The sticking zero-bias conductance peak feature when only one QD potential is varied around the sweet spot is clearly reproduced in G_{RR} of panel **b**. The quadratic peak splitting profile when both QD potentials are varied by the same amount is also reproduced the panel **d**. The left N contact of this device was broken and a distant lead belonging to another device on the same nanowire was used instead. This and gate jumps in V_{RD} complicate interpretation of other panels.



Extended Data Fig. 9 | CAR-induced and ECT-induced interactions across several QD resonances. a,**b**, Local (I_L) and nonlocal (I_R) currents as a function of V_{LD} and V_{RD} measured with V_{PG} = 200 mV and fixed V_L. All resonances show an ECT-dominated structure and a negative correlation between the local and the nonlocal currents. **c**,**d**, Local (I_L) and nonlocal (I_R) currents as a function of V_{LD} and V_{RD} measured with V_{PG} = 218 mV and fixed V_L. Some resonances show the structure associated with the $t = \Delta$ sweet spot, showing both positive and negative correlations between the local and nonlocal currents. **e**,**f**, Local (I_L) and nonlocal (I_R) currents as a function of V_{LD} and V_{RD} measured with V_{PG} = 200 mV and fixed V_L. All orbitals show a CAR-dominated structure and a positive correlation between the local and the nonlocal currents. All measurements were conducted with V_L = 10 μV, V_R = 0 and B = 100 mT.



Extended Data Fig. 10 | Theoretical effect of tunnel broadening on the charge-stability diagrams. In some charge-stability diagrams in which level repulsion is weak, such as Fig. 2a and Extended Data Fig. 4, some residual conductance is visible even when $\mu_{LD} = \mu_{RD} = 0$. This creates the visual feature of the two conductance curves appearing to 'touch' each other at the centre. In the main text, we argued that this is owing to level broadening. Here we plot the numerically simulated charge-stability diagrams at zero temperature under various dot-lead tunnel coupling strengths. We use coupling strengths $t = 20$ μV and $\Delta = 10$ μV as an example. From panels **a**–**c**, increasing the tunnel coupling and thereby level broadening reproduces this observed feature. When the level broadening is comparable with the excitation energy, $|t - \Delta|$, finite conductance can take place at zero bias. This feature is absent in, for example, Fig. 2c, in which $|t - \Delta|$ is greater than the level broadening.